Film Cooling Extraction Effects on the Aero-Thermal Characteristics of Rib Roughened Cooling Channel Flow

Beni Cukurel
e-mail: cukurel@vki.ac.be

Claudio Selcan
e-mail: selcan@vki.ac.be

Tony Arts
e-mail: arts@vki.ac.be

von Karman Institute for Fluid Dynamics,
Chaussée de Waterloo, 72, B-1640,
Rhode-St-Genèse, Belgium

The present study is geared towards quantifying the effects of film cooling holes on turbine internal cooling passages. In this regard, tests are conducted in a generic stationary model, with evenly distributed rib-type perturbators at 90 deg, constituting a passage blockage ratio of $H/D_h = 0.3$ and pitch-to-height ratio of $P/H = 10$. The 1/3H diameter surface-perpendicular film cooling holes are employed at a distance of 5/3H downstream of the preceding rib. Through liquid crystal thermometry measurements, the aero-thermal effects of a change in suction ratio are contrasted for various configurations ($Re = 40{,}000$ $SR = 0$–6), and compared with the analogous aerodynamic literature, enabling heat transfer distributions to be associated with distinct flow structures. At increased suction ratio, the size of the separation bubble downstream of the rib is observed to diminish, triggering globally an earlier reattachment; in addition to low-momentum hot fluid extraction via film cooling suction. Hence, in the presence of active flow extraction, higher overall heat transfer characteristics are observed throughout the channel. Moreover, the findings are generalized via friction factor and Nusselt number correlations, along with an analytical 20-pitch passage model. $SR \sim 3.5$ is observed to provide favorable characteristics of pitch-to-pitch uniform suction ratio, lack of hot fluid ingestion and to sustain the highest passage averaged heat transfer. [DOI: 10.1115/1.4007501]

Introduction

In anticipation of increasing efficiencies of modern gas turbine engines, the strong drive for higher compression ratios and turbine inlet temperatures significantly augments the thermal load on hot-gas components. To prevent damage due to excessive metal temperatures, up to 30% of the high-pressure compressor air is employed to cool down the early turbine stages exposed to the extreme combustor exit temperatures, where the thermodynamic efficiency penalty due to compressor air bleed out is outweighed by the gains in the Brayton cycle.

Based on internal forced convection, pressurized coolant air is routed through various cooling channels and is ultimately discharged into the external hot gas path, thereby extracting thermal energy from the airfoil. These serpentine passages are commonly equipped with repeated flow perturbators (ribs are the most common) in order to enhance convective heat transfer by promotion of turbulent mixing. However, an increase in surface roughness implies a trade-off between heat transfer enhancement and pressure drop penalty, and subsequently indicates a compromise between higher turbine inlet temperatures and more compressor air consumption. A multitude of extensive prior studies have quantified the aero-thermal characteristics of various rib geometries in terms of empirical correlations on heat transfer and friction factor with respect to geometric and aerodynamic parameters such as rib height, pitch, angle-of-attack, channel aspect ratio and Reynolds number.

In addition, to protect the outer layer of the turbine blade from gas temperatures beyond the material limit, external film cooling is also commonly employed. Forming a thin layer of insulation between the hot gas mainstream flow and the exposed blade surface, the coolant is extracted from the turbulated internal cooling channel walls via bleeding holes connecting the internal passages to the exterior. The film cooling performance is typically characterized by the film hole discharge coefficient, the adiabatic film effectiveness, and its effects on the blade internal and external local heat transfer. The film hole discharge coefficient relates the actual hole mass flow rate to the case of isentropic flow expansion; and it has a significant effect on the thermal performance of the hole, as well as the aerodynamic mixing losses [1]. Some of the main contributing factors are the hole location with respect to the turbulator, shape and angle of the hole and surface roughness. Despite its importance in design calculations, this parameter is mainly set by the geometry; and thus, it is not the present focus.

The adiabatic film effectiveness is associated with the efficiency of the coolant flow coverage over the blade external surface. Although there has been a significant amount of studies parametrically analyzing the effectiveness of film cooling on the external flow, investigations focusing on internal coolant flow heat transfer implications are limited in number.

The experimental flow field analysis of a two-pass squared ribbed channel, in the presence of film cooling suction, indicated flow extraction to introduce significant alterations to local velocity profiles and secondary flow structures [2]. A numerical simulation of coolant flow around a bleed hole investigated the flow impingement in the near hole region; the better performance of 90 deg over 150 deg angled holes was attributed to higher impingement and less coolant deviation [3].

Among the few studies in prior literature, Thurman and Poinsatte [4], and Shen et al. [5] experimentally studied the flow reattachment and local heat transfer enhancement effects of bleed flow extraction at different hole to channel mass flux ratios (suction ratios, SR) and hole locations. For bleed holes located in between the ribs, increased suction ratios cause higher surface

Contributed by the International Gas Turbine Institute (IGTI) of ASME for publication in the Journal of Turbomachinery. Manuscript received June 28, 2012; final manuscript received August 5, 2012; published online November 2, 2012. Editor: David Wisler.

heat transfer in the near hole region while globally augmented heat transfer enhancement can be achieved via an increase in Reynolds number [4]. Uniform suction ratio among all consecutive bleed holes; in contrast to ramped increasing or decreasing, yielded the highest overall heat transfer [4]. Bleed hole placement near the upstream rib is determined to be favorable for local heat transfer enhancement, [4] attributed to the suction of the separated flow region downstream of a rib; hence reduction of the recirculation bubble size and earlier reattachment [5]. Regarding thermal stresses, the introduction of bleed holes was found to increase the spanwise temperature uniformity [6].

Characterizing the internal cooling channel performance in an average sense, Han [7,8] presented empirical heat transfer and friction factor correlations derived from parametrical investigations for squared and rectangular ribbed passages, in the absence of film cooling holes. Taslim et al. [6] conducted experiments in a ribbed trapezoidal passage with bleed flow extraction, reporting empirical correlations for heat transfer. An extensive study by Kim et al. [9] investigated the effect of rib angle and suction ratio variation on heat transfer enhancement and friction factor. Moreover, channel rotation induced Coriolis force effects were studied on leading and trailing edge walls. Comparing the ribs positioned at 45 deg and 90 deg, for increased bleed flow, the slanted ribs were reported to produce reduced heat transfer; in contrast to the transverse ribs yielding enhanced values. For flow perpendicular ribs, both passage rotation and bleed flow extraction result in friction factor reduction, as well as heat transfer augmentation [9].

The endeavor of the current effort is to thoroughly investigate the aero-thermal problem of a rib roughened channel flow in the presence of extraction holes. The more generalized nature of the investigation is an effort to establish the aero-thermal fundamentals for enhanced understanding, as well as establishing a CFD validation case, rather than constituting a test case of an industrial contract for a pre-existing geometry. It is merely geared towards an application where this phenomenon is most common in practice, namely turbine blade cooling passages. Thus, to quantify the friction factor and aero-thermal effects of film cooling holes on internal cooling passages, pressure-drop and liquid crystal thermometry measurements are conducted on a scaled test section, modeling the features of a typical high blockage ratio ribbed channel geometry with film cooling suction.

The current geometry (absent of cooling holes) has previously been investigated in several studies at the von Karman Institute, each focusing on a different aspect of the problem, with added complexity [10–13]. The current heat transfer study builds upon this complementary database of information, acquired by the experimental and numerical prior work. Considering the early onset of many industrial design decisions, the establishment of a CFD validation case is imperative. Utilizing this database of information, the aerodynamic, thermal and pressure-loss effects of a change in suction ratio are contrasted for various configurations, and compared with the prior aerodynamic PIV and LES studies. The analysis attempts to generalize the findings to provide global guidelines towards ramifications of film cooling rate on internal channel flow.

Experimental Facility

The experimental facility is the simplified stationary model of a generic turbine internal cooling channel that is scaled up by a factor of 15. The channel comprises the inlet, test and exit sections, with each section formed of 100×100 mm cross sections with longitudinal dimensions of 800, 1400, 600 mm, respectively. The inlet and exit sections of the channel are made of smooth walls. In addition, for measurements conducted under various film cooling conditions, the test facility features a low pressure settling chamber, situated adjacent to the channel side wall, for film cooling suction. The entire model is built in Plexiglas, due to its favorable properties, such as optical transparency in the visual spectrum, high abrasion and ultraviolet resistance and low thermal conductivity. The basic schematic of the test facility is presented in Fig. 1.

Upstream of the channel, a honeycomb with 3 mm cell size is used along with a NACA bellmouth to provide flow conditioning. In gas turbine cooling passages, even though the aerodynamic flow development initiates in the root section of the turbine airfoil, the part of the cooling passage which promotes heat exchange is the serpentine passages. The test section segment of the facility models a portion of a serpentine, away from entry and turn effects. Thus, the unheated aerodynamic development length in the inlet section may provide a certain level of boundary layer similarity with the real engine environment. The exit section is connected to a chamber with three layers of honeycomb structures employed to damp out the fluctuations created by the blower which is situated downstream and facilitates a continuous steady air intake.

Experimental Test. The centrally located test section is assembled from four flat Plexiglas pieces, where only one of these surfaces contain rib-type perturbators. Situated perpendicularly to the mean flow direction, at an angle of attack of 90 deg, evenly distributed square ribs yield a configuration with a channel blockage ratio of $H/D_h = 0.3$, and a rib pitch to height ratio of $P/H = 10$. Despite being eventually a bit large for the intended application of turbine cooling passages, except for a few cases of very small engines where the manufacturing limitations might inflict larger rib size in smaller turbine components, the large blockage ratio (30%) is mainly adopted due to the fundamental nature of the study. The increased rib height not only results in large flow structures, which are easier to identify/measure/quantify, but also allows greater resolution in various measurement techniques. Moreover, since the integrity and details of the data are proportional to the size of the model, the selected configuration is a compromise between resolution and the available electrical power to heat the channel walls.

In addition to the rib perturbators, the third and fourth pitches of the test section are equipped with a set of cylindrical film cooling holes connecting the cooling channel with an adjacent settling chamber, Fig. 1. The air flow through these holes mimics the extraction of the internal coolant towards the external surface of a real turbine blade. The 1/3H diameter holes are employed at an angle of 90 deg with respect to the mean flow direction and are situated 5/3H downstream of the preceding rib center plane. The location of the film cooling holes is consistent with the investigations of Thurman and Poinsatte [4], who experimentally showed that placing the holes near the preceding rib ($\sim$1.6H) significantly enhances heat transfer, attributed to the removal of the separated flow near the downstream edge of the rib. Moreover, the flow perpendicular orientation of the cooling hole is consistent with the observations of Scheepers and Morris [3], who demonstrated the internal heat transfer benefits of the 90 deg configuration over the 150 deg orientation.

When a portion of the mass flow is sucked out by film cooling holes, a pitch to pitch periodicity cannot be established due to constant reduction in pitch-to-pitch flow rate, and thus local Reynolds number. The circumstance of having active upstream film cooling holes, at the penalty of ambiguous mass flow rate over the measured third pitch domain, is counterproductive. At the exit section, a butterfly valve enables the adjustment of relative mass flux rates between the mainstream and the bleeding holes; hence defining the channel and the cooling hole mass fluxes; the ratio of which is termed "suction ratio" (SR).

Over the ribbed surface, in order to impose an almost uniform heat flux distribution along the wetted solid-fluid interface, the entire ribbed wall facade (including the rib top and sides) is heated by means of a 25 μm thick Inconel sheet, connected to a 16 V–150 A dc power supply. The current is dissipated as thermal energy by the Joule effect and, at steady state, the heat is convected away primarily by the fluid in contact. The voltage applied across the foil is measured at the two longitudinal edges, whereas

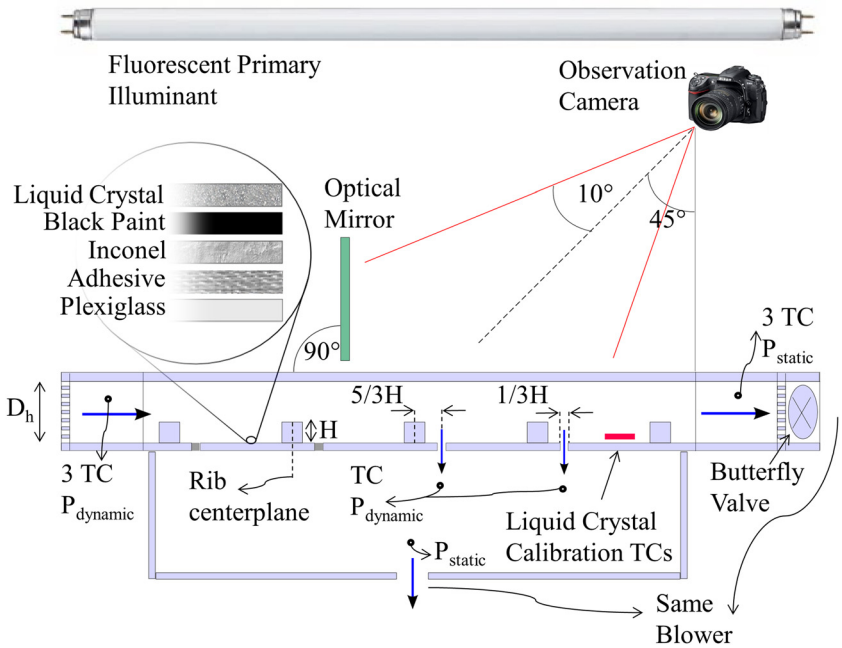

Fig. 1 Schematic of the experimental setup

the current is calculated by a shunt placed in series with the foil. For surface temperature measurements, micro-encapsulated cholesteric wide-band thermochromic liquid crystals (TLCs), type R35C20W by Hallcrest Inc., are employed. To yield optimal performance during the experiment, in terms of color brilliance and contrast, the TLC is deposited on a black underlying paint layer, Fig. 1. The test section is observed by a Nikon D300S camera.

In order to yield the optimal performance during experiment and calibration, a camera off-axis illumination configuration is used to minimize surface reflections, shadows and overcome issues of nonuniformity. The OSRAM type T8 L 36 W fluorescent light is mounted along the principal axis and above the side walls of the test surface, irradiating at a vertical distance of 1 m to the TLC surface.

During the measurements, it is more favorable to acquire the entire surface color distribution in a single image at a fixed angle consistent with the calibration. Therefore, aligned with the channel, the camera faces the upstream direction at 45 deg, where the upstream face of the rib is viewed by a 98% reflectance optical mirror, placed perpendicularly to the channel. Therefore, all planes such as the inter-rib space, the upstream, top and downstream faces of the rib; in addition to the mirror reflected channel view, are sustained at a uniform angle, where the viewing angle variation is confined to ± 10 deg.

Both, the camera and the mirror, are mounted on the same assembly, which is placed on a traversing mechanism, enabling the motion parallel to the setup. The parallel longitudinal motion of the observation assembly enables the switch between the passages designated for calibration (fourth pitch) and data acquisition (third pitch), without changing the angle between the components with respect to one another; this is favorable, considering the angular dependence of liquid crystals. To correlate the observed TLC colors with temperature, four Omega CO1-K type cement-on surface thermocouples are flush mounted onto the fourth inter-rib pitch in a crosshair configuration. This results in a confined exposed surface at the center.

Pressure and Flow Temperature Measurements. Immediately upstream and downstream of the test section, static pressure is measured on three faces of the channel, and averaged pneumatically. Moreover, the inlet section is modified for an access hole to introduce a total pressure probe. The film cooling hole performance is quantified via the prevailing static pressure in the adjacent chamber and a Kiel-head probe placed inside each jet core, 1.5 diameters downstream of the orifice exit. The steady pressure measurements are conducted by Validyne Model Dp10 transducers with replaceable diaphragms. The dynamic pressure is measured by Kiel head probes experimentally tested to be less than 1% sensitive to flow angle variations up to ± 25 deg.

Along with pressure measurements, freestream air temperature is measured via exposed T-type thermocouples located at inlet and exit sections and in the chamber downstream of the bleeding holes. The air temperature is monitored for setting the operating condition of the channel, as well as to estimate the local bulk flow temperature in the measurement domain.

The flow immediately downstream of the inlet duct is used as a reference point for calculating Reynolds number, based on hydraulic diameter of the inlet section and on the bulk flow velocity. The suction ratio is calculated as the hole to channel mass flux ratio, $\mathrm{SR} = \rho u_{\mathrm{hole}}/\rho u_{\mathrm{channel}}$ local to each pitch; the deviation between the third and fourth pitch film cooling hole mass fluxes is measured to be less than 5%, and thus the third pitch value is used for consistency. Pressure drop measurements are conducted within a range of $10{,}000 < \mathrm{Re} < 80{,}000$ and for $1.0 < \mathrm{SR} < 7.5$.

Hue-Temperature Calibration. The thermochromic liquid crystal calibration procedure is carried out in the fourth inter-rib passage. Since the reflectance properties of the mirror are slightly wavelength dependent, altering the hue of the observed image, the color response of the TLC section observed via direct and reflected views, is not identical. Thus, two independent hue-temperature calibration curves, one for the direct and one for the reflected portions of the image, have to be formulated separately in order to yield accurate results.

A background subtraction methodology is employed such that prior to the activation of the liquid crystals, an initial background image is captured at ambient conditions. The recorded inactivated TLC tristimulus values are used as a bias and subtracted in the RGB domain from every subsequently sampled image. When this procedure is employed, the calibration curves obtained for the various camera inclinations are all acceptable single valued hue angle relations [14]. Moreover, the viewing angle variations of magnitude

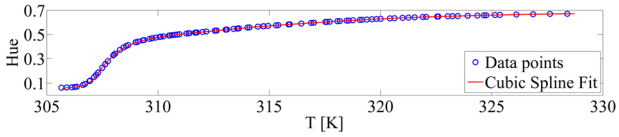

Fig. 2 Typical hue temperature calibration curve

± 15 deg, around the camera angle 45 deg, do not significantly alter the hue relation, all within ± 0.3 K [14].

The calibration is performed under natural convection and the test section is incrementally heated up from the lower to the upper limit of the TLCs active bandwidth. In order to establish the relationship between TLC color response and temperature, the readings from the surface thermocouples are recorded simultaneously as the image is captured by the camera. Then, the hue angle attribute can be calculated by employing Eq. (1),

$$H = \tan^{-1}\left[\sqrt{3}\cdot(G-B)/(2R-G-B)\right]/2\pi \tag{1}$$

Within the reference zone, the temperature readings of the surrounding thermocouples along with the regional hue values can be averaged, resulting in a typical calibration curve, Fig. 2. The discrete data is fitted by a monotonically increasing twice differentiable cubic spline with 20 knots.

Image Processing. Under various testing conditions, the Inconel covered wetted wall is heated up such that the minimum observed temperature is slightly above the TLC event clearance temperature and the surface temperatures are confined within the liquid crystal bandwidth. Due to the inclined optical path, all sampled images are significantly affected by perspective distortions. Hence, each region of the image is separately mapped and projected onto a single plane via independent bicubic transformations. The magnification factor varies along the test section due to the optical path; as an overall indicator, the averaged mean scale factor is calculated to be 12 pixels/mm.

During data acquisition, color images of the test surface are initially recorded in terms of tristimulus values of the digital camera. From each active RGB image, its correspondent background image is subtracted, and converted to local hue values. By the use of two separate calibration curves (direct and mirror view), the acquired hue-angle distributions yield the desired surface temperatures. Finally, the raw temperatures are processed via a series of median/symmetry/Gaussian low pass filters. The resulting temperature distribution is reconstructed in such a manner that it better reflects the generic behavior of a ribbed passage, Fig. 3. The resultant data are the combination of information extracted from the top and downstream faces of the third rib along with the third passage inter-rib space and upstream face of the fourth rib.

Local Heat Flux Estimation Around a Hole. Even though thin planar Inconel sheets are known to generate uniform Joule heating, under circumstances of local geometric singularities, there exist confined local heat flux deviations from this homogeneous behavior; in this case, it is attributed to the presence of film cooling holes. A coupled simulation is performed utilizing the COMSOL software to characterize the Joule heating problem in a FEM solver. The geometrical model is a planar representation of the Inconel surface which includes the bleeding hole openings. Stretched in the streamwise direction, it reproduces the original flat shape of the 25 μm thin sheet body. The governing equation for Joule heat generation is $-\nabla\cdot d(\sigma\nabla V)=0$, where d is the Inconel layer's thickness, σ is the electrical conductivity, V is the electrical potential, and ∇ denotes the gradient operator in the streamwise and lateral directions. The heat power per unit area produced inside the thin layer is given by $q_{\text{gen}} = d\sigma|\nabla V|^2$ and appears as an inward surface flux. Electrical insulation is imposed

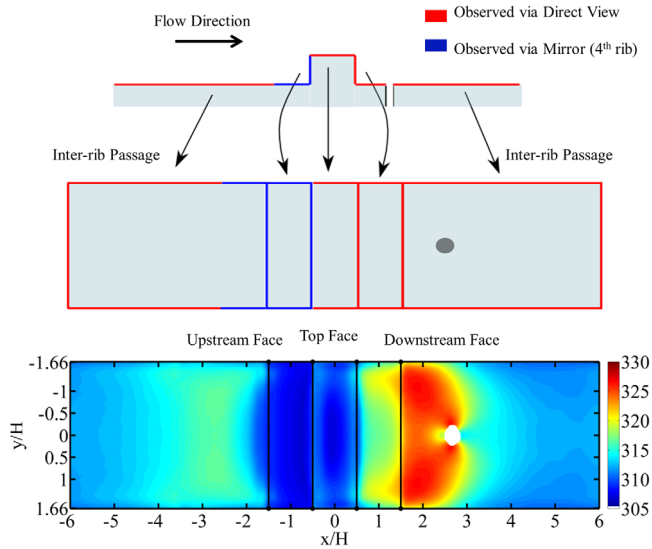

Fig. 3 Convective ribbed wall perspective mapping

at every exterior and interior edge, except for the longitudinal ends of the model where the Inconel foil is connected to the dc power source.

A key parameter in modeling the Joule heating effect is the electrical conductivity of the Inconel foil $\sigma = A_S/(R_{\text{in}}\cdot A_{\text{CS}}\cdot W)$ where A_S and A_{CS} denote the net surface area and the cross-sectional area of the Inconel sheet; W is the width, and R_{in} presents the actual electrical resistance of the Inconel foil. In this case, the electrical conductivity of the Inconel sheet is determined to be $\sigma = 953{,}006$ S/m, consistent with the manufacturer provided values.

At steady state, the resistive layer locally dissipates the heat on the surrounding fluid at $T_\infty = 300$ K, and through conduction within the thin sheet. The resulting temperature distribution on the exposed surface, T_s, is computed by the simultaneously solved conduction equation, $\nabla\cdot(-k\nabla T)=0$. The thermal conductivity of Inconel is $k = 14.9$ (W/m K).

While solving the FEM model, adiabatic thermal boundary conditions are applied to all external boundaries. On the stretched wetted surface of the foil, measurement representative heat transfer coefficients are uniformly imposed. Only to assess the heat redistribution, this approach estimates the local significance of convective heat transfer with respect to conduction within the foil.

Solving the Joule heating and conduction equations over a triangular meshed FEM model, the COMSOL routine computes the local redistribution of outward heat flux over the Inconel foil. Lastly, to preserve generality, the flux distribution can be normalized by the nominal mean value, yielding a single generic rib pitch, Fig. 4. Even though the heat flux is computed to be homogenous in a global sense, there exist local deviations in the vicinity of the film cooling holes. Due to concentration and divergence of iso-current lines around the hole, the characteristic flower heat flux pattern is created. Peak heat generation at the hole lateral edges are contrasted by local minima in the longitudunal current stagnation points, Fig. 4. Moreover, the redistribution of heat flux diminishes to less than 1% after six hole diameters. Thus, the local flux variations are significant around the hole; hence, accounted for in the subsequent calculations.

Local Heat Flux Estimation Around a Rib. In addition to the local heat flux deviations driven by the hole, the heat may not be convected directly away by the fluid in contact and locally there can be regions of slight redistribution within the Plexiglas body ($k = 0.18$ (W/m K)).

To acquire the surface heat flux, a single pitch of the Plexiglas ribbed wall, as well as the thin Inconel foil over the test section, is

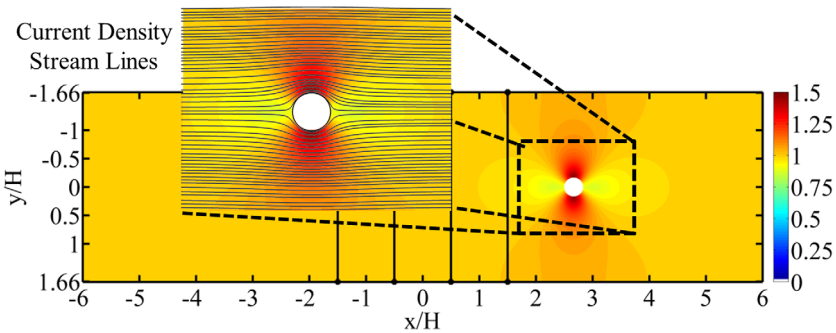

Fig. 4 Normalized heat flux distribution around a hole

modeled by the FEM solver. The COMSOL code solves the 2D Fourier conduction equation throughout the model to compute the temperature distribution inside the solid body. The boundary conditions of the problem are uniform heat generation within the Inconel body, a typical heat transfer coefficient distribution from Ref. [10] over the solid-fluid interface, adiabatic upstream and downstream vertical walls, and natural convection on the external bottom wall.

The resulting solid heat flux redistribution, normalized by the Inconel generated ideal flux, can be found in Fig. 5. At steady state, although the applied surface heat flux is mostly convected away by the fluid in contact, not only there exist slight redistribution effects, but back-face conduction losses of the order 4% are also observed. For longitudinal positions 0.5 H away from the rib, the solid conduction in the longitudinal direction constitutes less than ~1.5% of the surface value. Within the rib, this value may be as high as 4%, and at the rib downstream corner, there exists a localized deviation up to 12%. Therefore, the predictions of the FEM model are employed in a 2D sense to correct for these local deviations.

Enhancement Factor Calculation. From the liquid crystal thermometry measured surface temperatures, it is possible to calculate the local heat transfer coefficient,

$$h(x,y) = q(x,y)/(T(x,y) - T_\infty) \tag{2}$$

where T_∞ is the thermocouple measured air bulk temperature along the channel axis, experimentally verified to vary linearly from inlet to exit and considered as constant within a pitch. The surface heat flux distributions are obtained from COMSOL, where the local redistribution and losses of the Inconel foil flux are modeled. Subsequently, the computed heat transfer coefficient is nondimensionalized as a Nusselt number, $\mathrm{Nu} = h(x,y)D_h/k_f$, where D_h is the channel hydraulic diameter and k_f is the thermal conductivity of air.

In order to quantitatively assess the impact of artificial roughness elements on internal cooling channel performance, and thus to determine the relative heat transfer enhancement, the Nusselt number is normalized with respect to an empirical heat transfer correlation, $\mathrm{EF} = \mathrm{Nu}(x,y)/\mathrm{Nu_o}$. The denominator of the enhancement factor is obtained from the Dittus-Boelter equation, $\mathrm{Nu_o} = 0.023\mathrm{Re}^{0.8}\,\mathrm{Pr}^{0.4}$, a correlation for computing the local Nusselt number for hydrodynamically and thermally fully developed turbulent flows in smooth circular tubes valid for $0.7 < \mathrm{Pr} < 160$, $\mathrm{Re_{Dh}} > 10^4$, and $L/D_h > 10$.

Uncertainty. The measurement uncertainty is estimated with a single sample uncertainty analysis based on the method proposed by Kline and McClintock [15]. The overall uncertainty in wall temperature measurements can be decomposed in terms of uncertainty due to thermocouple reading (±0.35 K), hue contribution of the fixed broadband image noise (±0.25 K), angular dependency of the liquid crystals (±0.3 K), and deviation from the hue-temperature curve fit formulation (±0.2 K). This results in a combined wall temperature uncertainty of (±0.55 K). The major contributor to the heat flux uncertainty is the back face conduction losses. Although represented in the FEM model (Fig. 5), the natural convection heat transfer coefficient, as well as the back side freestream temperature, is largely unreliable; this could yield deviations from the model up to ±2%. Along with uncertainty on measured flow temperature, air thermal conductivity, and hydraulic diameter, the resulting nominal Nusselt number error is ±4%. Moreover, the error associated with Reynolds number is computed to be in the order of ±3.3%, while the subsequent EF uncertainty being ±4.8% in the 95% confidence interval. For pressure loss correlations, the friction factor error is estimated as ±6%.

Rib Roughened Channel Flow Field

Principal Flow Structures. Despite the geometric simplicity of the model, the employed step disturbance elements inside the

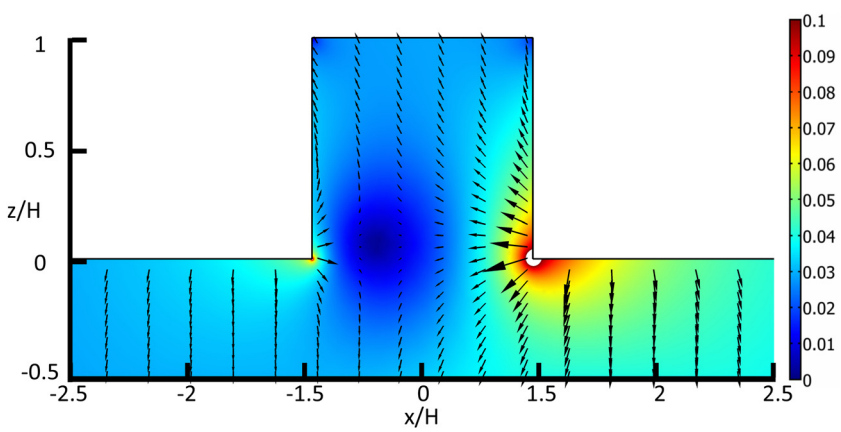

Fig. 5 Normalized heat flux distribution around a rib

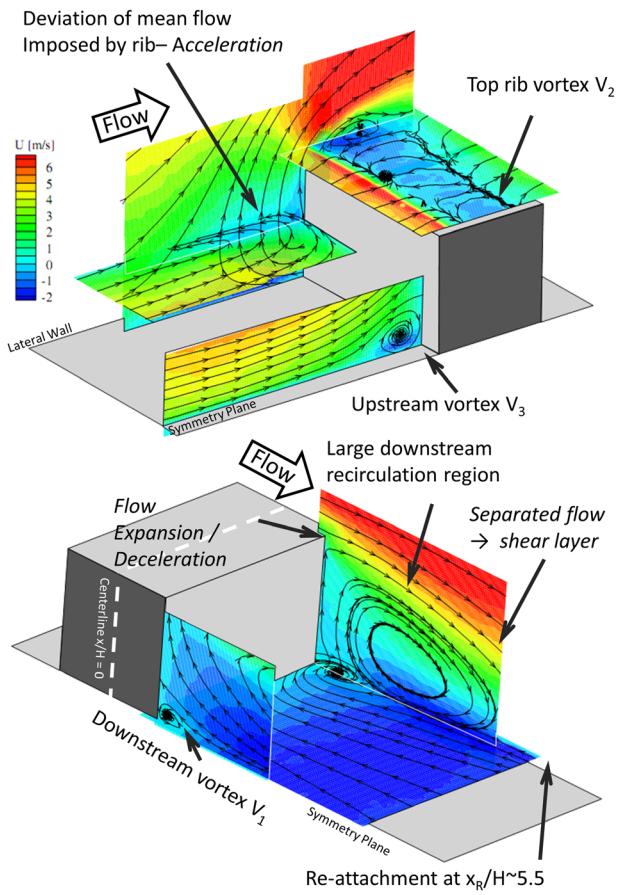

Fig. 6 Visualization of the ribbed channel flow field [11]

channel introduce a number of complex flow features into the mean stream. The examples of which can be found in a complementary PIV investigation [11], absent of film cooling holes, in Fig. 6, where time-averaged stream-traces along with longitudinal velocity contours are presented. The geometric configuration coincides with the present effort.

As the fluid encounters the rib, it experiences a strong deviation imposed by the obstacle, forcing it to adapt to the decreased channel cross section. It is accelerated in order to pass the rib and subsequently experiences an expansion further downstream as the cross-sectional area abruptly increases following the backward face of the rib. At the investigated Reynolds number, since the contribution of the inertial terms into the momentum balance is dominating, the fluid flow is not able to follow the abrupt changes of the surface. It is the sudden enlargement of the channel downstream of the perturbator which causes the stream to separate from the surface. A free shear layer is formed upon the separation of the upstream boundary layer at the sharp corner, due to the interaction between the mainstream flow and the reverse flow downstream of the rib. In a time-averaged sense, the region beneath the separated flow in the wake of the rib is occupied by a recirculation zone, with its length confined by the back face of the rib and the point of reattachment. In the region of flow reattachment, the separated shear layer curves sharply downward and impinges on the wall. When subjected to the effects of stabilizing curvature and a strong interaction with the wall, the shear layer is split into two fractions [16,17]. Since the energy of the first part does not suffice to overcome the strong adverse pressure gradient, it is deflected upstream; being reversed, it forms the recirculating flow region. The second part of the shear layer is carried away downstream, and contributes to the growth of a new sub-boundary layer, as it reattaches to the wall [16].

In this case, defined by the change of sign in skin friction coefficient, the reattachment point is determined to be around $x/H \sim 5.5$ rib heights downstream of the rib center-plane. The direct relation of the flow reattachment region with the local heat transfer distribution has been extensively studied in literature and the position of the maximum in the streamwise local Nusselt number profile, $x_{\max}$, has been considered a significant indication of flow reattachment, x_R [18,19].

Apart from this recirculation region, the flow field exhibits a local separated flow region V_2 on top of the perturbator, rotating CW, as well as a small CCW vortex cell V_1 in the rib downstream wall corner [11], both spanning across the entire channel width. This corner vortex V_1 and the recirculation region exhibit opposite mean angular velocities. Towards the obstacle, the stream traces of V_1 and the recirculation region coincide, such that the flow impinges onto the downstream surface of the rib.

Further downstream, the mean flow passes the rib and the subsequent recirculation zone, and impinges towards the bottom channel wall in the reattachment region. Once the flow reattaches, the boundary layer redevelops and grows within the inter-rib spacing, until the next turbulator. The stream strongly impinges on the vertical surface such that its vorticity and the repeatedly induced separation of the boundary layer give rise to the CW rotating vortex structure V_3 [11].

Film Cooling Hole Effect. The introduction of alternating film cooling holes to the inter-rib spacing induces major changes to the flow topology. In order to identify the aerodynamic implications of cooling flow extraction on the rib-roughened flow field, a complementary LES investigation is conducted in the same geometry including 1/3H diameter surface-perpendicular holes located at a distance of 5/3H downstream of the preceding rib [13]. The findings are contrasted with the prior observations at a hole to channel mass flux ratio (suction ratio) of 4.5.

A qualitative analysis by means of time averaged streamline charts yields valuable insight concerning the distortions imposed by the suction effect of the film cooling hole, noticeably affecting the region situated downstream of the rib obstacle. A three-dimensional visualization of stream traces for the configurations with and without a film cooling orifice can be found in Fig. 7.

In the absence of film cooling holes, comparing the LES (Fig. 7(*a*)) with the PIV (Fig. 6), there appears to be a high degree of qualitative correlation in the observed flow structures. With the film cooling orifice located at $x/H = 5/3$, clearly submerged entirely into the prior dominant recirculation bubble, the prevailing predicted local suction effect can be viewed in Fig. 7(*b*). The flow in the vicinity of the hole is continuously entrained and sucked out, thereby inducing significant distortions to the separated flow region and successive reattachment.

For the passage with the film cooling hole, the flow field downstream of the rib is primarily dominated by a flow characteristic that can be addressed as a type of bifurcation mechanism. By splitting the fluid entrained in the prevailing recirculation region, the portion of the flow structure below 1/3H height is transported along the bottom wall and entrained by the suction of the hole. The flow above this zone experiences an abrupt upward lift dominated by the shear layer driven vorticity. Being initially shed away downstream over the orifice, it exhibits a reverse flow motion while descending again behind the hole. After impinging on the channel bottom wall, the fluid is again diverted upstream due to the suction effect and thus likewise entrained by the orifice.

The green stream trace surface represents flow propagation of fluid from the downstream face of the rib. Accumulated by the recirculating behavior of the separation bubble, the mainstream flow near the channel lateral wall is entrained and transported to the back side of the rib. Ascending under the effect of the upward flow motion, it interacts with the channel mainstream flow, and thus forms a part of the free shear layer. It is evident that the stream traces corresponding to the configuration with cooling hole exhibit a higher curvature than in the case without, and are bent towards the wall. Thus, since the orifice acts as a potential sink for

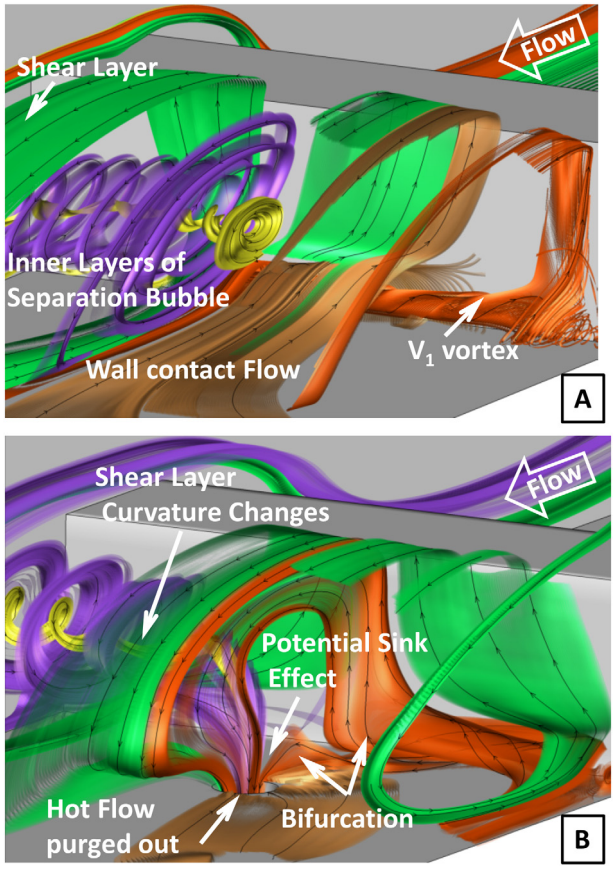

Fig. 7 Rib downstream flow (*a*) without film cooling hole (*b*) with film cooling hole [13]

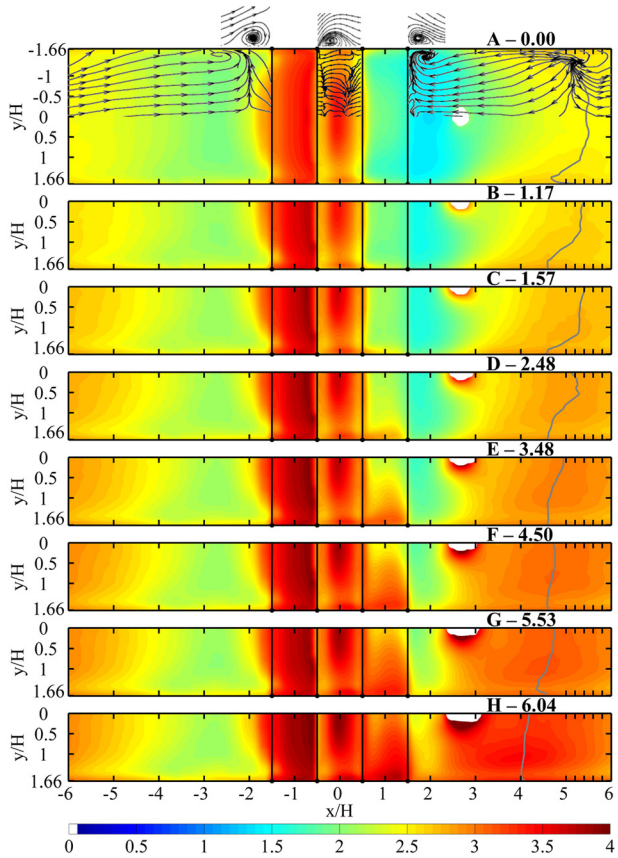

Fig. 8 Effects of suction ratio on EF distributions

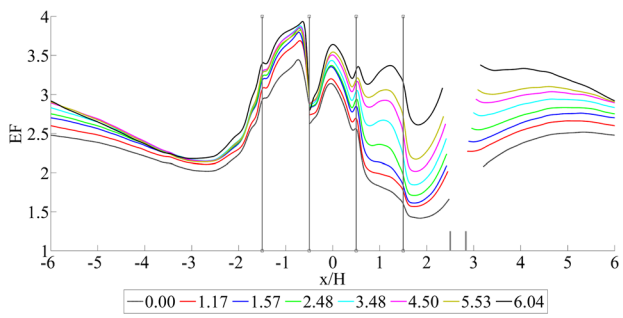

Fig. 9 Laterally averaged EF at various suction ratios

the locally separated low momentum fluid, the reattachment line is deformed and shifted further upstream; this trend is expected to be amplified at increased suction rates.

The development of the vortex structure V_1, exemplified by the orange stream traces, appears to be distorted due to bifurcation in the presence of the film cooling hole. In contrast to the case lacking an active film cooling hole, the flow is significantly diverted towards the symmetry plane, and experiences a sudden upward rise and subsequent entrainment by the orifice suction effect.

The inner layers of the recirculation bubble, purple and yellow surfaces, exhibit the characteristic vortical motion within the separation bubble in addition to the spanwise translational motion. In the presence of film cooling suction, Fig. 7(*b*), under the potential sink effect, the structures seem to be extracted directly through the hole in the symmetry plane.

Apart from the aerodynamic flow topology, the fluid in contact with the bottom wall (the brown surface in Fig. 7) has possible heat transfer connotations due to its relation with the local thermal boundary layer. In the absence of the film cooling hole, fluid heated by the bottom and lateral walls is observed to be entrained by the separation region and to persist in the recirculation bubble, thereby isolating the region downstream of the rib against penetration of cool mainstream flow. In contrast, with active film cooling holes, high temperature fluid near the passage bottom wall is eventually entrained by the suction effect and extracted out of the channel, whether directly or after interaction with V_1. The removal of the hottest fluid layers from the passage could have beneficial internal heat transfer ramifications.

Results

In order to investigate the aerothermal effects of film cooling holes on the internal cooling channel, liquid crystal experiments are conducted. The holes carry the flow out of the test section at suction ratios of SR = 0, 1.17, 1.57, 2.48, 3.48, 4.50, 5.53, and 6.04. The SRs yield bleed ratios (BRs), defined as the fraction of the channel mass flow extracted by the film cooling hole suction at a given pitch, of 0.92%, 1.23%, 1.95%, 2.73%, 3.53%, 4.34%, 4.74%. Figure 8 presents enhancement factor distributions along the ribbed test section for all investigated operating conditions, while the gray lines represent the location of the streamwise maximum heat transfer in the vicinity of the reattachment zone. Furthermore, providing a more global perspective, Fig. 9 depicts the laterally averaged EF evolutions.

Baseline Ribbed-Roughened Flow Heat Transfer. Considering the characteristic flow patterns developing inside internal ribbed cooling channel geometries and analyzing the results obtained from the liquid crystal experiments, some distinctive heat transfer distributions can be correlated to nearby flow structures. Figure 8(A) presents the EF distribution in the absence of suction,

SR = 0. In addition, on the upper half of the heat transfer map, the bottom wall nearest PIV stream traces are shown, along with the symmetry plane V_3, V_2, and V_1 vortex structures located in front of, over, and behind the rib respectively [11].

The region confined by $-6 < x/H < -4.5$, situated downstream of the large recirculation, is characterized by a zone where the attached flow exhibits a gradual boundary layer development, supported by an overall slight decrease in enhancement factor in the axial direction. Within this region, even though the flow resembles a state of unperturbed boundary layer development over a flat plate, the elevated enhancement factor, EF ~ 2.4, is mainly due to higher than ordinary local turbulence levels [18]. The turbulent skin friction fluctuation intensity is observed to be of the order 100%–120%, in contrast to the case of a typical turbulent boundary layer over a flat plate with an intensity of the order 40% [18].

Further downstream, the convective heat transfer is greatly influenced by the potential effect of the rib. Reduction in the flow streamwise velocity, generally associated with boundary layer thickening, results in the initial drop in enhancement factor, $-4.5 < x/H < -2.5$ region. This effect is less emphasized in the lateral direction due to aerodynamic wall effects, $1.2 > |y/H|$. The portion of the inter-rib area directly upstream of the front face of the rib, bounded by $-2.5 < x/H < -1.5$, is under the influence of the clockwise rotating corner vortex formation V_3. The increased entrainment of colder fluid causes a steep rise in enhancement factor up to EF ~ 3 on the channel bottom surface in the direct proximity of the rib.

The upstream face of the rib ($-1.5 < x/H < -0.5$), is an area characterized by globally high enhancement factors attributed to the strongly impinging mainstream flow. This high-momentum impinging flow, guided by the V_3 vortex, causes a peak in heat transfer, EF ~ 3.5, at $x/H \sim -0.8$. The top surface of the perturbator, bounded by $-0.5 < x/H < 0.5$, is another region where large EFs are observed due to the rib blockage driven reduction in effective flow area, in turn locally augmenting the flow velocity. This is particularly true for the symmetry plane where the mass flux is largest. EF values, around 3.4, are reduced in the lateral direction, indicated by lower heat transfer levels of EF ~ 3.2 at $|y/H| = 0.83$ and EF ~ 2.8 at $|y/H| = 1.66$. Within this region, the location of the distinct peak appears to be related to the aerodynamic throat and the V_2 flow structure, creating a local maximum towards the rib centerline, Fig. 9.

Regarding the EF distribution over the vertical back face of the rib, $0.5 < x/H < 1.5$, a significant drop in EF is observed from around EF ~ 2.5 at the top rib edge, $x/H = 0.5$, to EF ~ 1.5 at the bottom corner, $x/H = 1.5$. The adjacent bottom surface of the inter-rib section, directly in the wake of the obstacle, $1.5 < x/H < 2$, exhibits a similar trend. Here, the reduction in EF is even more remarkable, indicated by a local minimum of EF ~ 1.3 at $x/H = 2$ for $|y/H| < 1.4$. The entire section of distinctively reduced heat transfer rates downstream of the flow perturbator, $0.5 < x/H < 2.5$, is induced by the separated and recirculating flow behind the rib. The recirculation bubble, not only prevents the entrainment of fresh fluid, but also generates a local low momentum region with reversed flow orientation and thus particularly low levels of effective heat transfer. This trend of sharp reduction is apparent in the entire width.

Further downstream of the rib, $2.5 < x/H < 6$, the EF begins to increase monotonously as cooler flow is progressively entrained from the mainstream, a consequence of the diminishing rib wake effects. At an increased axial position, eventually, the mainstream flow becomes once again attached to the bottom surface, indicated by a change of direction in stream-traces at around $x/H \sim 5.5$ in Fig. 8(A). Even though the maximum heat transfer can occur downstream or upstream of the aerodynamic reattachment point, as a qualitative indicator, the maximum inter-rib space EF in the longitudinal direction is indicated by the gray line in Fig. 8. The PIV acquired stream traces and the liquid crystal heat transfer results seem to agree on the location of the reattachment region and this point is demonstrated to slightly vary in the lateral direction, from around $x/H \sim 5.4$ in the symmetry plane to $x/H \sim 4.8$ towards the lateral walls. Downstream of the reattachment point, considering the periodicity of the flow structures, the cyclic behavior perpetuates.

Comparing the general longitudinal EF trends of the present investigation, Fig. 9, with the investigations of Metzger et al. [20] for similarly high blockage ratios channels (25%) equipped with ribs at 90 deg and $P/H = 10$, a great deal of similarity can be observed. Consistent with the present study, the findings indicate slight decrease in Nusselt number downstream of the reattachment, from $x/H = -6$ to $x/H = -1.5$, followed by monotonous heat transfer increase over the upstream face of the rib. On top of the rib, the Nusselt number stagnates, then augments, and finally decreases sharply, which persists over the back face of the rib. In agreement with the current findings, the immediate rib downstream region is associated with the lowest heat transfer rates, followed by a gradual increase towards the reattachment.

From a more global perspective, locally area averaging EF maps in various zones of the present rib roughened geometry, the mean EF for the rib upstream face, the rib top face, the rib downstream face, the inter-rib spacing are computed to be 3.20, 2.86, 1.89, 2.20, respectively, resulting in a global area averaged EF of 2.31. Consequently, the highest heat transfer zones are the upstream and top faces of the rib.

Film Cooling Hole Suction Effects on Local EFs. In order to isolate the internal cooling heat transfer ramifications of film cooling holes at channel Reynolds number of 40,000, the "baseline case" without any film cooling suction, Fig. 8(A), is compared with the EF distributions in the presence of an active film cooling hole at various suction ratios Figs. 8(B)–(H) for SR = 1.17, 1.57, 2.48, 3.48, 4.50, 5.53, and 6.04, respectively. Moreover, for each operating condition, Table 1 summarizes the regionally averaged EFs; in addition to providing the surface percent standard deviation of EF from the global mean; hence quantifying the nonuniformity. Furthermore, the reattachment associated maximum heat transfer locations, x_{max}, are presented for the symmetry line.

In Figs. 8(A)–(H), through qualitative comparison of the distributions associated with various suction rates, it is apparent that the cooling flow extraction significantly alters the heat transfer in the channel. At increased film cooling suction rates, for all regions of the ribbed passage, the enhancement factor monotonously augments, Table 1. For SR = 0 and SR = 6.04, the surface averaged EF increases from 2.31 up to 2.98. The backward face and inter-rib surface seem to be the zones mostly affected by this suction effect, evidenced by a percent change in mean EF of 73% and 29%, respectively, from SR = 0 to SR = 6.04, Table 1. In contrast, the upstream and top faces of the rib are not as sensitive to a change in suction rate, exhibiting a moderate EF alteration of 15% and 16%.

In an attempt to highlight the aero-thermal phenomena driving these observed trends, the local EF distributions found in Fig. 8 are examined along with the prior described flow topology. With the increased suction rate, it is clear that the size of the separation bubble diminishes; this is indicated by the monotonous streamwise decrease in reattachment length, suggested by the shift in reattachment maximum heat transfer point from $x/H = 5.45$ to 4.20, Table 1, Fig. 8. This is related to the hole suction effect, changing the curvature of the shear layer, inducing a potential sink like behavior on the locally separated low momentum fluid. In the lateral direction, for the case without film cooling holes, towards the lateral walls, the reattachment occurs earlier with respect to the center plane. In the presence of film cooling suction, at increased suction ratio, the reattachment line (x_{max}), represented by the gray lines in Fig. 8, is more uniform (flatter) in the lateral direction.

In addition to flow reattachment considerations, there exist the complementary benefits of low momentum hot fluid extraction, evidenced by the EF augmentation at $1 < x/H < 2$ for increased suction

Table 1 Summary- flow extraction effect on channel EF

		Region averaged EFs							
		Rib							
Bleed ratio per pitch	Suction ratio	Ups.	Top	Downs.	Mean	Inter rib	Pitch ave.	% Stand. dev.	x_{max}
0	0	3.20	2.86	1.89	2.65	2.20	2.31	20.0%	5.45
0.92%	1.17	3.42	2.94	2.04	2.80	2.34	2.45	18.6%	5.41
1.23%	1.57	3.51	3.06	2.18	2.92	2.42	2.54	18.5%	5.40
1.95%	2.48	3.56	3.09	2.37	3.00	2.48	2.61	17.5%	5.12
2.73%	3.48	3.61	3.15	2.63	3.13	2.57	2.71	16.7%	4.95
3.53%	4.5	3.61	3.22	2.88	3.23	2.64	2.79	16.0%	4.73
4.34%	5.53	3.60	3.25	3.01	3.28	2.69	2.84	15.6%	4.72
4.74%	6.04	3.69	3.33	3.27	3.43	2.83	2.98	16.3%	4.20
	$\Delta EF/EF_{SR0}$	15%	16%	73%	29%	29%	29%		

rates. In the absence of film cooling, owing to the isolated stagnant behavior of this low momentum region, the local wall-interface fluid temperature is relatively high, yielding a low heat transfer zone. The suction effect not only reenergizes the flow, but also, through enhanced interaction with the surrounding structures, the isolation of this zone diminishes and the wall interface fluid temperature is expected to decrease, both contributing to the observed higher heat transfer rates. For lower suction ratios up to 3.48, the average EF over the entire pitch is higher than on the rib downstream face, where the lowest EF factors are observed, Table 1 and Fig. 9. At higher hole suction rates, this trend reverses, and rib downstream face, performs better than average (2.88 with respect to 2.79) for SR = 4.50, indicating a significant extraction of the low momentum fluid.

In the absence of cooling holes, the rib downstream face is the region of the flow field which is dominated by the recirculation zone and the associated CCW rotating V_1 vortex. For SR ≥ 2.48, there seems to be a local peak in heat transfer at around $x/H = 1.15$, Fig. 9. Though not conclusive, this could be an indication of the bifurcation mechanism strengthening the V_1 vortex, which in turn impinges on the rib side wall with a greater downwash momentum, creating a local maximum in enhancement factor. In the lateral direction, the region close to the lateral wall on the rib downstream face, Fig. 8(A) $0.5 < x/H < 1.5$ and $1 < y/H < 1.66$, exhibits a local minimum in heat transfer. In contrast, in the presence of film cooling, Figs. 8(B)–(H), this region is characterized by a locally higher enhancement factor, with this effect being emphasized at higher SR.

On the surfaces surrounding the hole, $|x/H - 2.67| < 0.7$ and $|y/H| < 0.7$, heat transfer peaks are generated by the local acceleration of the fluid from all directions, Fig. 8. In comparison, the local effect of the film cooling hole seems to decrease at increased axial distance from the hole. Specifically, for points downstream of the reattachment zone, the heat transfer rates gradually converge for all mass flux ratios until they roughly coincide at $x/H = -2.8$. This is the region of the inter-rib space where the flow is dominated by the potential effect of the rib, resulting in a mostly unchanged distribution indicated by the broad collapse of the EF lines.

Further downstream, $-2.8 < x/H < -1.5$, higher suction rates still result in higher EFs despite the earlier flow reattachment and thus the more developed thermal boundary layer, Fig. 9. For an increase in suction ratio, the detrimental effects of the augmentation in thermal boundary layer thickness, associated with an earlier reattachment, are contrasted by the probable *local* increase in velocity magnitude. This suggested augmentation in local momentum flux is based on the flow fields having similar static pressure for all operating conditions, but at increased suction with the reduction in flow back pressure created by the hole, the flow can be presumed to accelerate at a greater rate. This effect can also be observed on the upstream and top faces of the rib, $-1.5 < x/H < 0.5$, where there is a self-similar distribution augmentation in EF at increased suction rates.

Within the tested operating condition limits, from a pure internal heat transfer perspective, it seems favorable to augment the suction rate as much as possible to benefit from the monotonously higher EFs. Yet, the other consideration is the temperature uniformity of such a cooling configuration. In the case of thermal investigations for which the boundary condition is iso-heat-flux at the fluid-solid interface, the temperature uniformity is directly proportional to the uniformity in EF. Within the scope of the tested mass fluxes, at first, increasing film cooling suction not only augments the heat transfer rate, indicated by the rise in overall EF in Table 1, but also forces the surface temperature distribution to become more uniform, denoted by the drop in EF percent standard deviation. This is beneficial to prevent thermal gradients. At higher than 5.53 suction ratios, even though the global heat transfer rate continues to increase, the heat transfer distribution begins to be more nonuniform, apparent from the rise in EF deviation to 16.3% at SR = 6.04. Contrary to the general declining EF deviation trend from SR = 0 to SR = 5.3, this would yield greater thermal gradients for larger suction ratios.

Generalization to Multi-Pitch Channels

In an attempt to extend the implications of the experimentally acquired single pitch heat transfer data, a cooling channel is analytically modeled up to 20 pitches (each with cooling holes) to reflect broader trends. Assuming the first pitch Reynolds number and suction ratio are known, and the film cooling hole exit pressure is uniform along the span (reasonable considering the blade span-wise orientation of the cooling channel principal axis), and by keeping all geometric parameters the same, one can compute Reynolds number and local suction ratio at each hole.

Conservation of mass in a single pitch domain provides

$$\mathrm{Re}_{i+1} = \mathrm{Re}_i(1 - \mathrm{SR}_i\mathrm{AR}) \tag{3}$$

Applying Bernoulli's equation on a stream tube connecting the hole and the proceeding pitch yields

$$\tilde{P}_{i+1} + \mathrm{Re}_{i+1}^2/2 = \tilde{P}_h + \mathrm{SR}_i^2\mathrm{Re}_i^2/2 \tag{4}$$

and the conservation of energy in a domain surrounding a full passage pitch provides

$$\begin{aligned}&\left(\tilde{P}_i + \mathrm{Re}_i^2/2\right) - \left(\mathrm{Re}_{i+1}/\mathrm{Re}_i\right)\left(\tilde{P}_{i+1} + \mathrm{Re}_{i+1}^2/2\right)\\ &\quad - (\mathrm{SR}_i\mathrm{AR})\left(\tilde{P}_h + \mathrm{SR}_i^2\mathrm{Re}_i^2/2\right) = \bar{f}L/D_h\mathrm{Re}_i^2/2\end{aligned} \tag{5}$$

where $\tilde{P}$ is the nondimensional pressure, SR is the hole suction ratio, AR is the hole to channel area ratio, and $\bar{f}$ is the pitch average

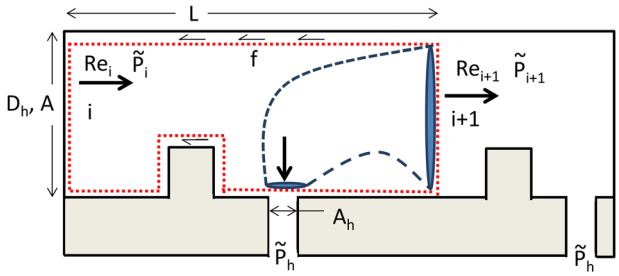

Fig. 10 Generalized cooling hole setup—control volumes

Darcy friction factor. The schematic of the control volumes can be found in Fig. 10.

Solving the three equations simultaneously, one can compute Re_2, $\tilde{P}_h$ and $\tilde{P}_2$ in the first pitch ($i=1$); and for a constant $\tilde{P}_h$, the equations are then solved for Re_{i+1}, $\tilde{P}_{i+1}$, and SR_i in the remaining pitches. The only remaining unknown in this model is the Reynolds number dependent friction coefficient. In the absence of film cooling, tests are conducted with the current experimental facility at various Reynolds numbers and the total pressure drop across the channel is monitored. It has been shown in Ref. [7] that the mean friction factor is merely a geometric average of the smooth and ribbed face friction coefficients, in this case $\bar{f}=(3f_s+f_r)/4$. The smooth square channel friction factor has been demonstrated to be no more than 4% different from the Blasius solution for smooth circular tubes [7], which provides $f_s=0.184Re^{-0.2}$. Then, the acquired 17 different pressure drop measurements over a range of Reynolds numbers can be found in Fig. 11.

With a maximum deviation from the curve fit of the order of 2%, the resulting normalized ribbed face friction factor is

$$f_r/f_s = 1.7461 \times 10^{-4}\ Re + 39.344 \tag{6}$$

valid within $10^4 < Re < 8 \times 10^4$. For the current configuration the friction factor effect due to the existence of the rib with respect to the smooth channel is in the order of 50-fold. At Reynolds number 40,000, this results in channel averaged friction factor ($\bar{f}/f_s$) of 12, consistent with observations in Ref. [10].

Further experiments are conducted to characterize the friction factor in the presence of a film cooling hole (f_{rh}); in this regard, the third pitch suction hole is activated for various Reynolds numbers at numerous suction ratios. For each of the 42 data points taken, the average friction factor, the smooth face friction factor and thus the mean ribbed face friction factor can be computed from the total pressure drop, upstream Reynolds number and suction rate. Considering the geometric distribution of ribbed passages with and without film cooling holes, one could estimate the ribbed surface friction factor in the presence of a film cooling hole using

$$f_{rh}(Re_i) = 5\bar{f}_r - 2f_r(Re_i) - 2f_r(Re_{i+1}) \tag{7}$$

The consequent normalized friction factor can be found in Fig. 11, and is characterized as

$$f_{rh}/f_r = \left(10^{10}Re^{-3.306} - 4.692 \times 10^{-4}\right)\left(SR^{3.28} - 1934\right) \tag{8}$$

valid for $10^4 < Re < 8 \times 10^4$ and $1.0 < SR < 7.5$. The mean curve fitting error is 2.5% and is bounded by a maximum of 6%. Expectedly, f_{rh} is lower than f_r due to the decrease of the low momentum area downstream of the rib.

Having characterized the friction coefficients for various Reynolds numbers and suction ratios, one could easily solve the system of equations. Within the scope of this exercise, constrained by the present geometry and simplified modeling assumptions, it may be possible to project the single passage data to yield broader observations. Using the series of equations, for a given set of initial conditions with $Re_1=40{,}000$ and $SR_1=0$, 1.0, 1.5, 2.0, 2.5, 3.0, 3.5, 4.0, the analytical cooling channel model is solved to provide local pitch-to-pitch suction ratios up to 20 pitches, Fig. 12.

For $SR_1 \leq 3.0$, along the streamwise direction, as the pitch number increases, the suction ratio reduces with respect to its initial level. More specifically, due to low initial starting levels of pressure in the domain, defined by the prescribed initial conditions Re_1 and SR_1, at $SR_1=1$, 1.5, 2.0, 2.5, and 3.0, there is external hot flow ingestion into the internal cooling passage at the third, fifth, seventh, twelfth, and nineteenth pitch, respectively. In the absence of friction, due to constant total pressure and despite the loss of mainstream channel velocity, the flow velocity out of the hole remains constant; thus essentially increasing the suction ratio for the subsequent pitches. In the presence of friction losses, represented in this model as a static pressure drop, this behavior is mostly maintained for higher suction ratios ($SR_1=4.0$), since the initial difference between the internal and external pressure is higher under these circumstances. SR_1 equivalent to 3.5 seems to be the operating point where the suction ratio is most uniform between different pitches.

With the knowledge of local Reynolds and SR for each pitch, the passage heat transfer can be estimated, within the limitation of the analytical model. To accomplish this task, the global heat transfer coefficient is related to the present experimentally acquired eight suction ratios,

$$Nu(SR) = (0.01262\ SR + 0.2946)Re^{0.6397}\ Pr^{0.4} \tag{9}$$

In this equation, the Reynolds power dependence is calculated by the equations outlined in Ref. [8]. The maximum error associated with the linear Nusselt number versus suction ratio curve-fitting is computed to be 1.5%.

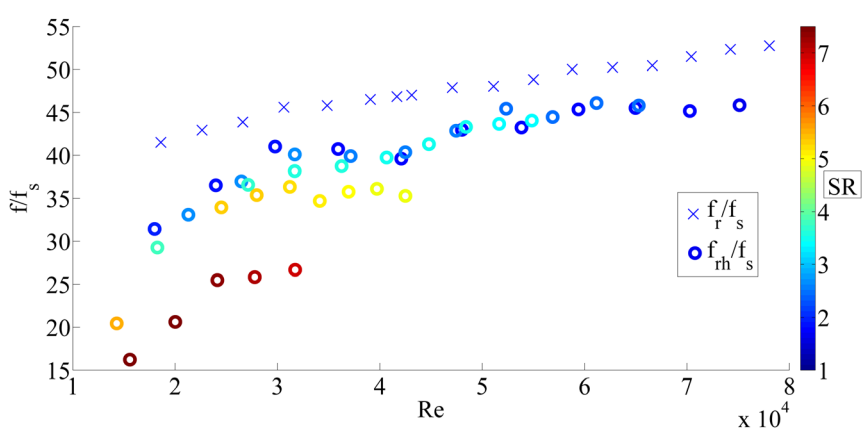

Fig. 11 Wall friction factor at various suction ratios

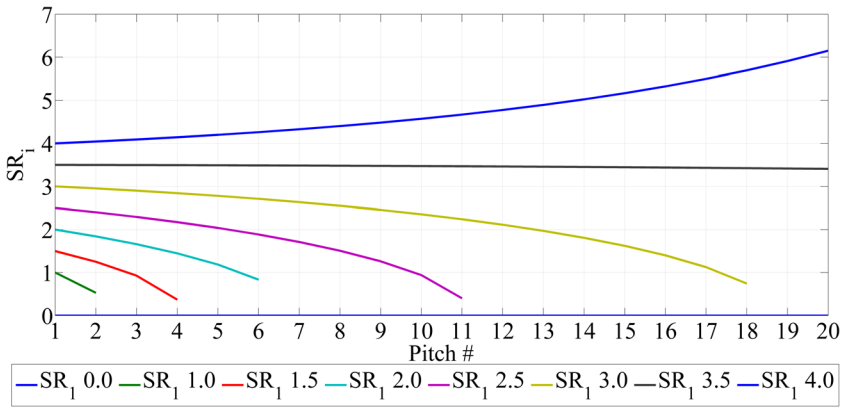

Fig. 12 20 Blade model—local SR at each pitch

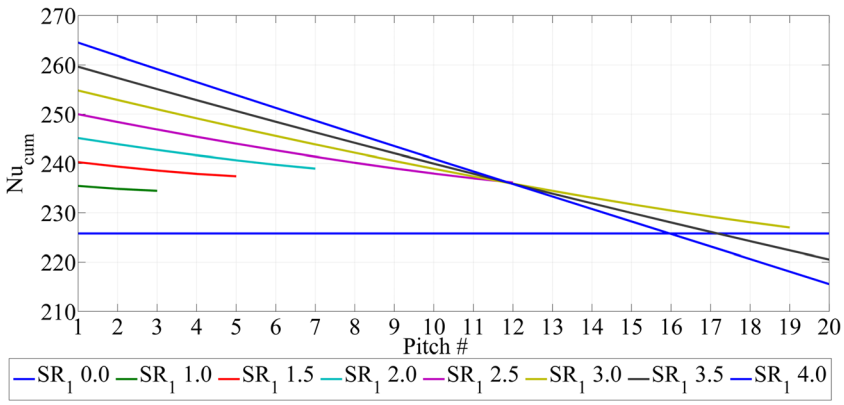

Fig. 13 Blade model—Nusselt number average up until each pitch

Considering the internal cooling considerations at various suction ratios, Fig. 13 presents the cumulative averaged Nusselt number up to the pitch of interest,

$$\mathrm{Nu}_{\mathrm{cum}} = 1/i \int_1^i \mathrm{Nu}_p \, dp \tag{10}$$

where Nu_p is the local Nusselt number associated with a given pitch. The horizontal line is associated to the case in the absence of any film cooling hole extraction. Due to the thermally beneficial aspects of the film cooling hole flow, all SR_1's are observed to be initially performing better than the baseline case. Eventually, the heat transfer reduces due to the drop in local pitch Reynolds number, Re_i. For $\mathrm{SR}_1 > 3.0$, despite an augmentation in suction ratio with increased pitch-wise position, Fig. 12, the dominant heat transfer effect is associated with the reduction in local mass flux, indicated by the negative slope in Fig. 13.

Depending on the number of pitches present in the cooling channel, one can find different optima in SR_1, such that for the first 12 pitches, higher SR_1 result in more favorable heat transfer characteristics. But for a channel consisting of more than 12 pitches, this trend reverses due to the high bleed of mass flow. The conditions with lower SR_1, if they are beyond the limit of ingestion, yield enhanced heat transfer behavior.

From an internal heat transfer perspective of this 20 pitch channel, Fig. 13, the optimal SR_1 is around 3.5 where the suction ratio is nearly uniform, there is no hot fluid ingestion and the highest average heat transfer rate is achieved. In agreement with the present findings, Thurman and Poinsatte indicated uniform suction ratio among all consecutive bleed holes; in contrast to ramped increasing or decreasing, to yield the highest overall heat transfer [4]. Furthermore, at this operating condition, due to the beneficial aspects of film cooling hole placement in the wake of the rib, the heat transfer performance of the internal cooling channel with and without film cooling are roughly the same, $\mathrm{SR}_1 = 0$ and $\mathrm{SR}_1 = 3.5$ in Fig. 13. Thus, the added benefit of blade external surface coolant coverage is gratis.

Conclusions

The mean flow field inside the rib-roughened cooling passage is complex and is characterized by distinct structures such as the rib downstream recirculation region, along with vortices located upstream, downstream and over the rib. In each region, distinctive heat transfer distributions, acquired by liquid crystal investigations, are correlated to nearby flow structures. The introduction of film cooling holes into the inter-rib spacing induces major changes to the flow topology, reflected as monotonous enhancement factor augmentation, for all regions of the ribbed passage. This effect is most prominent for the rib backward face and inter-rib space. For operating conditions where the suction ratio is greater than 3, the regions covered by the recirculation, perform better than the pitch average. At increased suction ratios, the importance of the separation bubble diminishes, triggering earlier reattachment; in addition to the complementary benefit of low momentum hot fluid extraction through the film cooling suction. From a pure heat transfer perspective, it seems favorable to augment the suction rate as much as possible to benefit from the monotonously higher EFs. However, for operating conditions $\mathrm{SR} > 5.5$, the heat transfer distribution begins to be more nonuniform, contrary to the general declining trend. This could result in greater thermal gradients in engine environment.

In an attempt to generalize the findings towards broader annotation, a cooling channel passage is analytically modeled up to 20 pitches. The system of equations is complemented by measured geometry specific friction factor correlations for the rib roughened wall, in the presence and absence of the film cooling suction. Associated with a smaller separation region, a reduction in friction factor is observed for the case with active film cooling. Moreover,

general longitudinal averaged channel heat transfer is correlated to local Reynolds number and suction ratio. Within the limitations of the model, from an internal heat transfer perspective of the 20 pitch channel, the optimal suction ratio of the first passage is demonstrated to be around 3.5. The suction ratio remains nearly uniform for the entire passage, and the described operating condition does not allow hot fluid ingestion and provides the highest complete passage averaged heat transfer rate.

Acknowledgment

The authors acknowledge the financial support of the Air Force Office of Scientific Research (AFOSR), Grant No. FA8655-08-1-3048, supervised by Dr. S. Surampudi and Dr. G. Abate of the European Office of Aerospace Research and Development. The authors also wish to thank F. J. G. Soto and C. Benocci for the LES calculation, supporting the flow field description.

Nomenclature

AR = hole to channel area ratio
BR = $m_{\text{hole}}/m_{\text{channel}}$ (bleed ratio)
CW = clockwise direction
CCW = counter-clockwise direction
D_h = channel hydraulic diameter
EF = $\text{Nu}/\text{Nu}_\text{o}$
f = Darcy friction factor
H = rib height
L = pitch length
LC = liquid crystal
LES = large eddy simulation
m = mass flow rate
Nu = Nusselt number
$\text{Nu}_\text{o} = 0.023\text{Re}^{0.8}\text{Pr}^{0.4}$ (Dittus Boelter corr.)
P = pressure
$\tilde{P} = P\rho D_h^2/\mu^2$ (nondimensional pressure)
PIV = particle image velocimetry
SR = $\rho u_{\text{hole}}/\rho u_{\text{channel}}$ (suction ratio)
Re = $\rho V D_h/\mu$ (Reynolds number)
TC = thermocouple
x = longitudinal distance from rib center-plane
x_R = reattachment distance
$x_{\max}$ = maximum Nusselt number location
y = lateral distance from symmetry line

Greek Symbols

ρ = density
μ = viscocity

Subscripts

h = hole
i = pitch number
r = ribbed surface
rh = ribbed surface with film cooling holes
s = smooth surface
cum = cumulative average up until a given location

References

[1] Bunker, R. S., and Bailey, J. C., 2001, "Film Cooling Discharge Coefficient Measurements in a Turbulated Passage With Internal Crossflow," ASME J. Turbomach., **123**(4), pp. 774–780.
[2] Chanteloup, D., and Bölcs, A., 2002, "Flow Characteristics in Two-Leg Internal Coolant Passages of Gas Turbine Airfoils With Film-Cooling Hole Ejection," ASME J. Turbomach., **124**(3), pp. 499–507.
[3] Sheepers, G., and Morris, R. M., 2009, "Experimental Study of Heat Transfer Augmentation Near the Entrance to a Film Cooling Hole in a Turbine Blade Cooling Passage," ASME J. Turbomach., **131**, p. 4.
[4] Thurman, D., and Poinsatte, P., 2001, "Experimental Heat Transfer and Bulk Air Temperature Measurements for a Multipass Internal Cooling Model With Ribs and Bleed," ASME J. Turbomach., **123**(1), pp. 90–96.
[5] Shen, J. R., Wang, Z., Ireland, P. T., Jones, T. V., and Byerley, A. R., 1996, "Heat Transfer Enhancement Within a Turbine Blade Cooling Passage Using Ribs and Combinations of Ribs With Film Cooling Holes," ASME J. Turbomach., **118**, pp. 428–434.
[6] Taslim, M. E., Li, T., and Spring, S. D., 1995, "Experimental Study of the Effects of Bleed Holes on Heat Transfer and Pressure Drop in Trapezoidal Passages With Tapered Turbulators," ASME J. Turbomach., **117**, pp. 281–289.
[7] Han, J. C., 1984, "Heat Transfer and Friction in Channels With Two Opposite Rib-Roughened Walls," ASME J. Heat Transfer, **106**, pp. 774–781.
[8] Han, J. C., 1988, "Heat Transfer and Friction Characteristics in Rectangular Channels With Rib Turbulators," ASME J. Heat Transfer, **110**, pp. 321–328.
[9] Kim, K. M., Park, S. H., Jeon, Y. H., Lee, D. H., and Cho, H. H., 2008, "Heat/Mass Transfer Characteristics in Angled Ribbed Channels With Various Bleed Ratios and Rotation Numbers," ASME J. Turbomach., **130**(3), p. 031021.
[10] Casarsa, L., Cakan, M., and Arts, T., 2002, "Characterization of the Velocity and Heat Transfer Fields in an Internal Cooling Channel With High Blockage Ratio," ASME Paper No. GT-2002-30207.
[11] Casarsa, L., and Arts, T., 2005, "Experimental Investigation of the Aerothermal Performance of a High Blockage Rib-Roughened Cooling Channel," ASME J. Turbomach., **127**(3), pp. 580–588.
[12] Lohász, M. M., Rambaud, P., and Benocci, C., 2006, "Flow Features in a Fully Developed Ribbed Duct Flow as a Result of MILES," Flow Turbulence Combust., **77**(1–4), pp. 59–76.
[13] Soto, F. J. G., 2011, "Investigation of Interaction of Coherent Structures on Heat Transfer in Ribbed Duct," von Karman Institute for Fluid Dynamics, Diploma Course Report.
[14] Cukurel, B., Selcan, C., and Arts, T., 2012, "Color Theory Perception of Steady Wide Band Liquid Crystal Thermometry," Exp. Therm. Fluid Sci. 2012, Vol. 39, pp. 112–122.
[15] Kline, S. J., and McClintock, F. A., 1953, "Describing Uncertainties in Single-Sample Experiments," Mech. Eng., **75**, pp. 3–8.
[16] Zukauskas, V. A., and Pedisius, K. A., 1987, "Heat Transfer to Reattached Fluid Flow Downstream of a Fence," Wärme- und Stoffübertragung, **21**, pp. 125–131.
[17] Eaton, J. K., and Johnston, J. P., 1981, "A Review on Subsonic Turbulent Flow Reattachment," AIAA J., **19**(9), pp. 1093–1100.
[18] Eaton, J. K., and Vogel, J. C., 1985, "Combined Heat Transfer and Fluid Dynamic Measurements Downstream of a Backward-Facing Step," ASME J. Heat Transfer, **107**, p. 922.
[19] Sparrow, E. M., Kang, S. S., and Chuck, W., 1987, "Relation Between the Points of Flow Reattachment and Maximum Heat Transfer for Regions of Flow Separation," Int. J. Heat Mass Transfer, **30**(7), pp. 1237–1246.
[20] Metzger, D. E., Chyu, M. K., and Bunker, R. S., 1988, "The Contribution of On-Rib Heat Transfer Coefficients to Total Heat Transfer From Rib-Roughened Surfaces," *Transport Phenomena in Rotating Machinery*, J. H. Kim, ed., Hemisphere, Washington, D.C.